JOURNAL OF PROPULSION AND POWER
Vol. 26, No. 1, January–February 2010

Sidewall Boundary Layers of the Bidirectional Vortex

Joshua W. Batterson* and Joseph Majdalani†
University of Tennessee Space Institute, Tullahoma, Tennessee 37388

DOI: 10.2514/1.40442

This study seeks to resolve the sidewall boundary layers forming in the axial and radial directions of a bidirectional vortex chamber. Our analysis is initiated by the formulation of the laminar boundary-layer equations via an order of magnitude reduction of the incompressible Navier–Stokes equations at the wall. Asymptotic theory is then applied to linearize and systematically truncate the governing equations, thus converting them from partial differential equations to more manageable ordinary differential equations. Scaling transformations are additionally applied to resolve the rapid changes arising near the sidewall. Because of the spatial character of the outer solutions, further transformations of the dependent variables are undertaken to secure the axially changing outer conditions. Through the use of matched-asymptotic expansions, we recover similar boundary-layer structures in all three orthogonal directions: the axial and radial components presented here, and the wall-tangential boundary layer obtained previously. This behavior is consistent with the resultant velocity being dominated by its tangential component and with the tangential boundary layer being axially invariant. These factors cause the axial layer to remain uniform in the streamwise direction. Based on the ensuing asymptotic results, viscous corrections at the wall are seen to be mainly dependent on the vortex Reynolds number, V. The latter combines the swirl number, the Reynolds number, and the chamber aspect ratio. Having obtained the three components of the velocity, essential flow characteristics, such as pressure, vorticity, swirling intensity, and wall shear stresses, are evaluated and discussed.

Nomenclature

A_i = inlet area
a = chamber radius
b = chamber outlet radius, $b < a$
l = chamber aspect ratio, L/a
p = normalized pressure, $\bar{p}/(\rho U^2)$
Q_i = normalized volumetric flow rate, $\bar{Q}_i/(Ua^2) = \sigma^{-1}$
$\bar{Q}_i$ = inlet volumetric flow rate
Re = injection Reynolds number, $Ua/\nu = 1/\varepsilon$
r, z = normalized radial or axial coordinates, $\bar{r}/a$, $\bar{z}/a$
S = swirl number, $\pi ab/A_i = \pi\beta\sigma$
s = scaled transformation variable, $(\pi - \eta)/\delta$
U = average inflow velocity in the tangential direction, $\bar{u}_\theta(a, L)$
$\boldsymbol{u}$ = normalized velocity $(\bar{u}_r, \bar{u}_z, \bar{u}_\theta)/U$
u_θ = normalized swirl/spin/tangential velocity, $\bar{u}_\theta/U$
V = vortex Reynolds number, $Q_i Re(a/L) = (\varepsilon\sigma l)^{-1}$
α = constant, $\frac{1}{6}\pi^2 - 1 \simeq 0.644934$
β = normalized outlet radius, b/a
δ = η minus rescaled layer
δ_w = wall boundary-layer thickness, $\bar{\delta}_w/a$
ε = perturbation parameter, $1/Re = \nu/(Ua)$
η = transformed variable, πr^2
κ = inflow parameter, $Q_i/(2\pi l) = (2\pi\sigma l)^{-1}$
ν = kinematic viscosity, μ/ρ
ρ = density
σ = modified swirl number, $Q_i^{-1} = S/(\pi\beta)$

Subscripts

i = inlet property
r = radial component
z = axial component
θ = azimuthal component

Superscripts

o = outer (inviscid) solution
$-$ = dimensional variables

I. Introduction

CHARACTERIZATION of unidirectional vortex flows has remained a central topic of interest since its earliest beginnings, marked by the work of Rankine [1] in 1858. Other notable advancements may be attributed to Lamb–Oseen [2,3], Burgers–Rott [4,5], Batchelor [6], and others. These basic flows remain valuable tools in modeling natural atmospheric and stellar phenomena [7,8]. For example, the Rankine vortex is still used as a crude approximation for describing the bulk motion of hurricanes and other large, atmospheric, swirl-dominated patterns. Jupiter's Great Red Spot is also regarded as a Rankine type vortex [9]. Lamb–Oseen and Burgers–Rott vortices are closely related in that they can both be defined in terms of a Gaussian function [10]. They become identical when suitably normalized, and both can be applied to localized atmospheric swirling flows such as tornados, dust devils, and water spouts [11]. As they are relevant to a variety of phenomenological applications, interest in their behavior continues to rise. The reader is referred in this regard to recent investigations by Alekseenko et al. [12], Eloy and Le Dizès [10], Schmid and Rossi [13], Olendraru and Sellier [14], Pérez-Saborid et al. [15], and others. Included among its pertinent applications, the Lamb–Oseen solution appears to be a viable model for trailing vortex streaks produced by lifting bodies and other such vortices that dissipate with time as a result of shear. These, however, are restricted to unidirectional vortex distributions.

A glimpse at bidirectional motion may be caught in Sullivan's 1959 solution of an external two-cell vortex [16]. Sullivan characterizes the swirl velocity in terms of integral functions and mates this profile with both axial and radial components. Common to all of these models is the existence of two fundamental regions: a forced vortex forming around the axis of rotation and a free vortex that is essentially irrotational. Whereas the free vortex is inviscid, the

Presented as Paper 4123 at the 37th AIAA Fluid Dynamics Conference and Exhibit, Miami, FL, 25–28 June 2007; received 15 August 2008; revision received 15 September 2009; accepted for publication 20 September 2009.

*Graduate Research Assistant, Mechanical, Aerospace and Biomedical Engineering Department. Member AIAA.
†H. H. Arnold Chair of Excellence in Advanced Propulsion, Mechanical, Aerospace and Biomedical Engineering Department. Senior Member AIAA.

character of the forced vortex is dominated by viscous stresses. In these models, the forced vortex diameter increases while the maximum swirl velocity diminishes with successive increases in viscosity (see Vatistas et al. [17–19]).

In the context of bidirectional flow, Bloor and Ingham [20] have analyzed the flow in cyclonic separators assuming a conical geometry that incorporates a vortex finder. Their solution, albeit inviscid, may be considered a milestone achievement in advancing the theory of confined swirl-dominated flows. Bloor and Ingham's motivation was industry driven, specifically geared toward cyclonic devices (see Fig. 1). These are widely used in the petrochemical, mineral, and powder processing industries. As for its application to rocketry, Chiaverini et al. [21–23] may be said to have pioneered the implementation of bidirectional swirl technology in the development of liquid rocket thrust engines, including the self-cooling vortex combustion cold-wall chamber (VCCWC).

The first exact solution to Euler's equations in reference to the VCCWC flowfield was developed by Vyas and Majdalani [24] directly from first principles. It was further extended to spherical geometry by Majdalani and Rienstra [25] and, to the treatment of conical cyclones, by Barber and Majdalani [26]. A complementary set of Eulerian solutions of the Beltramian type were later produced by Majdalani [27], who used the Bragg–Hawthorne equation as a starting point. These inviscid solutions resembled Bloor and Ingham's in exhibiting a singularity at the centerline. Shortly thereafter, viscous corrections were derived to overcome the swirl velocity's singularity at the origin and the no slip at the sidewall in the tangential direction [28]. Thus, with the exception of Bloor and Ingham [20], no other bidirectional vortex model has been advanced despite its relevance to both the propulsion and particle separation industries. Yet Bloor and Ingham's model remains, to this date, inviscid and singular at the vortex axis [20]. The same may be said of the class of Beltramian flows described in [27]. For this reason, the present article is aimed at developing an improved representation of the bidirectional vortex that secures the sidewall boundary layers in all three spatial directions: axial, radial, and tangential. The effort complements the work initiated in [28], which focused on the confined, complex lamellar vortex in a right-cylindrical chamber.

The viscous solutions of the bidirectional vortex, including those for the axial and radial velocities presented here, offer several unique attributes when compared to classic models arising in swirl-dominated configurations. The historical Rankine vortex, which is still employed in certain applications, remains overly simplistic. It exhibits a strictly one-dimensional character that takes no account of the inherent axial and radial velocities induced by the low-pressure region forming around its axis. Furthermore, its piecewise nature does not permit the smooth matching of its forced vortex core to its outer vorticity-free region. This is contrary to the present analysis in which a unifying, uniformly valid approximation of the bidirectional vortex is achieved through the use of matched-asymptotic expansions. Along similar lines, the Lamb–Oseen [2,3] and Burgers–Rott vortices [29,5] exhibit comparable swirl velocities although they remain limited to unidirectional motion. Bidirectionality is featured in Sullivan's unconfined vortex [16] and Bloor and Ingham's conical model [20]. However, the former is expressed using an integral formulation that limits its applicability whereas the latter, being inviscid, contains the usual singularity at the centerline. Furthermore, neither Sullivan's nor Bloor and Ingham's models seek to satisfy the physical requirement of no slip at a bounding wall. It can thus be seen that, unlike most historical models that discount the presence of an outer boundary, the confined bidirectional vortices under consideration entail, by necessity, viscous interactions with a chamber wall. The evaluation of viscous stresses becomes an integral requirement when considering roll torque, stability, and heat transfer. For more detail on this subject, the reader is referred to a survey on swirl-dominated motions by Batterson et al. [11].

Beyond the physical necessity to capture viscous effects, the work presented here details a novel mathematical procedure for matching solid surface interactions to a preexisting inviscid base flow. By systematically truncating the Navier–Stokes equations, compact boundary-layer equations are recovered. At the outset, a complicated set of coupled partial differential equations (PDEs) are reduced to a single, more manageable, independent set of ordinary differential equations (ODEs) for the boundary layers.

The accurate treatment of the problem's boundary layers is helpful in predicting several flow characteristics. These include the spatial evolution of the swirling intensity, the magnitude of the surface stresses, and the potential for roll torques. These can play an important role in the design of propulsive and guidance equipment. The viscous boundary layers are also a prerequisite for initiating a thermal analysis of this problem.

To engage the treatment of boundary layers at the confining sidewall, standard asymptotic techniques are applied to the yet-untreated radial and axial momentum equations. These will enable us to construct uniformly valid, matched-asymptotic approximations for the two remaining components of the velocity. We initiate the analysis by reducing the Navier–Stokes equations to recover Prandtl's boundary-layer equations [30]. We then follow Majdalani and Chiaverini [28] and Conlisk [31] in seeking asymptotic simplifications that ultimately lead to the desired solutions. We thus derive new expressions for the pressure distribution, shear stresses, vorticity, swirling intensity, and other characteristics of the boundary layers.

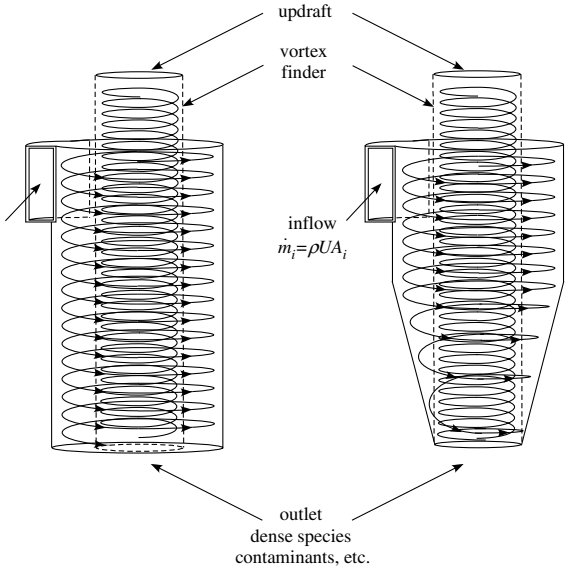

Fig. 1 Sketch of cylindrical (left) and conical (right) cyclone separators with heavy uses in industry.

II. Mathematical Formulation

The mathematical model, nomenclature, normalization, and coordinate system follow those employed by Majdalani and Chiaverini [28] (see Fig. 2). We recognize that the decoupled axial and radial profiles are characterized by different velocity and length scales than those affecting the tangential motion. Renormalization with respect to characteristic parameters in the longitudinal direction is not necessary as it will result in the same outcome. To remain consistent throughout, the original nomenclature is used here. Accordingly, spatial coordinates are normalized by the radius a, pressure by ρU^2, and velocities by the average wall-tangential

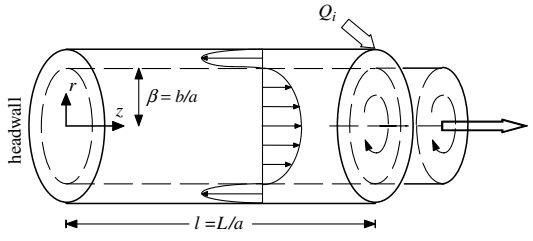

Fig. 2 Idealized chamber geometry and coordinate system.

injection speed U. As usual, the flow is assumed to be axisymmetric and steady. Our small viscous parameter ε is defined as $Re^{-1} \equiv \nu/(aU)$.

A. Axial Corrections

The axial boundary-layer equations can be obtained according to Prandtl's order of magnitude reduction applied to the cylindrical Navier–Stokes equations [30]. These are deduced by truncating at $O(\delta)$, where δ is the characteristic boundary-layer thickness. We consider $\varepsilon \sim \delta^2$, $r \sim \delta$, and $u_z \sim z \sim O(1)$. Furthermore, we assume that parallel flows evolve at $O(1)$ (Tetervin [32]). The boundary-layer equation can thus be rearranged and simplified. In nondimensional form, it can be written as

$$u_r \frac{\partial u_z}{\partial r} + u_z \frac{\partial u_z}{\partial z} = -\frac{\partial p}{\partial z} + \varepsilon\left(\frac{\partial^2 u_z}{\partial r^2} + \frac{1}{r}\frac{\partial u_z}{\partial r}\right) \tag{1}$$

with the conditions

$$\begin{cases} u_z(1, z) = 0 \\ \lim\limits_{r\to 0} u_z(r, z) = u_z^{(o)} \end{cases} \tag{2}$$

It should be noted that Eq. (1) represents Euler's axial momentum equation that has been modified by including the dominant components of viscous stresses. The concept of initiating the boundary-layer treatment from a regularized form of Euler's equations has, in fact, been used in similar physical contexts. Examples abound and one may cite, for example, the characterization of vorticity generated along the axis of a solid rocket motor by Balachandar et al. [33].

Here $u_z^{(o)} = 2\pi\kappa z \cos(\pi r^2)$ represents the outer solution that must be recovered as $u_z(r, z)$ leaves the near-wall region. To begin, the pressure gradient term is extracted from the inviscid solution, $\partial p/\partial z = -4\pi^2\kappa^2 z$. The inflow parameter κ is defined by Vyas and Majdalani [24] to be $\kappa = Q_i/(2\pi l) = (2\pi\sigma l)^{-1}$, where Q_i is the normalized volumetric flow rate and l is the aspect ratio, L/a. The inflow parameter varies with the reciprocal of the swirl number to the extent that, for a swirl-dominated flow, $\sigma l \gg 1$; the small relative size of κ justifies ignoring the axial pressure gradient. This will be later shown more formally using scaling analysis. Another simplification can be made here after Conlisk [31]. Noting that radial gradients dominate $(\partial/\partial r \gg \partial/\partial z)$, axial derivatives may be ignored. This assumption is further confirmed by the outer axial pressure and velocity gradients that are small relative to their radial counterparts. The final assumption concerns the outer radial velocity to be used to approximate the variable coefficient in the boundary-layer equation. Applying these assumptions to Eq. (1) delivers the compact form

$$\varepsilon \frac{1}{r}\frac{\partial}{\partial r}\left(r\frac{\partial u_z}{\partial r}\right) + \frac{\kappa}{r}\sin(\pi r^2)\frac{\partial u_z}{\partial r} = -4\pi^2\kappa^2 z \tag{3}$$

At this juncture, a useful variable transformation may be implemented. Letting $\eta = \pi r^2$ and $\partial/\partial r = 2\pi r \partial/\partial\eta$, substitution into Eq. (3) yields

$$\varepsilon\left(\frac{\partial^2 u_z}{\partial \eta^2} + \frac{1}{\eta}\frac{\partial u_z}{\partial \eta}\right) + \frac{\kappa}{2\eta}\sin(\eta)\frac{\partial u_z}{\partial \eta} = -\frac{\pi\kappa^2 z}{\eta} \tag{4}$$

To more easily confront the rapid changes near the wall we seek a scaling transformation that applies to the boundary-layer region (see Fig. 3). Because $r \to 1$ corresponds to $\eta \to \pi$, we select the stretched coordinate transformation

$$s = \frac{\pi - \eta}{\delta}; \qquad \eta = \pi - s\delta \tag{5}$$

We thus arrive at

$$\frac{\varepsilon}{\delta^2}\left(\frac{\partial^2 u_z}{\partial s^2} - \frac{\delta}{\pi - s\delta}\frac{\partial u_z}{\partial s}\right) - \frac{\kappa}{2\delta(\pi - s\delta)}\sin(\pi - s\delta)\frac{\partial u_z}{\partial s} = -\frac{\pi\kappa^2 z}{\pi - s\delta} \tag{6}$$

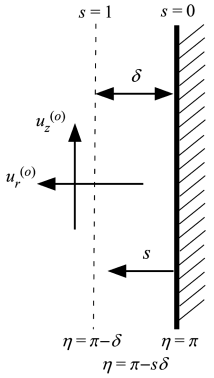

Fig. 3 Coordinate transformations in the sidewall boundary-layer region.

Next, we expand the variable coefficient into

$$\begin{aligned} -\frac{\kappa}{2\delta(\pi - s\delta)}\sin(\pi - s\delta) &\simeq -\frac{\kappa}{2\delta(\pi - s\delta)}\left[\pi - s\delta - \frac{1}{6}(\pi - s\delta)^3\right] \\ &= -\frac{\kappa}{2\delta}\left[1 - \frac{1}{6}(\pi - s\delta)^2\right] \simeq \frac{\kappa}{2\delta}\left(\frac{1}{6}\pi^2 - 1\right) \end{aligned} \tag{7}$$

Upon substitution into Eq. (6), we obtain the linearized form of the equation

$$\frac{\varepsilon}{\delta^2}\left(\frac{\partial^2 u_z}{\partial s^2} - \frac{\delta}{\pi - s\delta}\frac{\partial u_z}{\partial s}\right) + \frac{\kappa}{2\delta}\left(\frac{1}{6}\pi^2 - 1\right)\frac{\partial u_z}{\partial s} = -\frac{\pi\kappa^2 z}{\pi - s\delta} \tag{8}$$

Then, in an effort to counterbalance the key terms above, we take the distinguished limit to be $\delta \approx \varepsilon/\kappa$. This enables us to revisit Eq. (8) and eliminate the inhomogeneous and curvature terms at order ε. We extract

$$\frac{\partial^2 u_z}{\partial s^2} + \frac{\alpha}{2}\frac{\partial u_z}{\partial s} = 0; \qquad \alpha \equiv \frac{1}{6}\pi^2 - 1 \tag{9}$$

with the dual boundary conditions

$$\begin{cases} u_z(0, z) = 0 & \text{no slip} \\ \lim\limits_{s\to\infty} u_z(s, z) = u_z^{(o)} & \text{merging with outer solution} \end{cases} \tag{10}$$

Upon careful examination of the boundary conditions on the inner solution, we find it necessary to apply a transformation of the dependent variable, namely, $u_z = \xi_z(s)\pi z\cos(\pi - 2\pi s V^{-1})$; $V \gg 1$. In doing so, a constant limit is placed on ξ_z rather than the variable condition that plagues Eq. (10). In this vein, we first expand the derivatives and dismiss terms of order $V^{-1} \ll 1$. We collect

$$\begin{aligned} \frac{\partial u_z}{\partial s} &= -\pi z\cos(2\pi\frac{s}{V})\frac{\mathrm{d}\xi_z}{\mathrm{d}s} + 2\pi^2\frac{z}{V}\sin(2\pi\frac{s}{V})\xi_z \\ &\simeq -\pi z\cos(2\pi\frac{s}{V})\frac{\mathrm{d}\xi_z}{\mathrm{d}s} \\ \frac{\partial^2 u_z}{\partial s^2} &= -\pi z\cos(2\pi\frac{s}{V})\frac{\mathrm{d}^2\xi_z}{\mathrm{d}s^2} + 4\pi^2\frac{z}{V}\sin(2\pi\frac{s}{V})\frac{\mathrm{d}\xi_z}{\mathrm{d}s} \\ &\quad + 4\pi^3\frac{z}{V^2}\cos(2\pi\frac{s}{V})\xi_z \simeq -\pi z\cos(2\pi\frac{s}{V})\frac{\mathrm{d}^2\xi_z}{\mathrm{d}s^2} \end{aligned} \tag{11}$$

These turn Eq. (9) into

$$\begin{aligned} &-\pi z\cos\left(2\pi\frac{s}{V}\right)\frac{\mathrm{d}^2\xi_z}{\mathrm{d}s^2} - \frac{\alpha}{2}\pi z\cos\left(2\pi\frac{s}{V}\right)\frac{\mathrm{d}\xi_z}{\mathrm{d}s} = 0 \quad \text{or} \\ &\frac{\mathrm{d}^2\xi_z}{\mathrm{d}s^2} + \frac{\alpha}{2}\frac{\mathrm{d}\xi_z}{\mathrm{d}s} = 0 \end{aligned} \tag{12}$$

As for the boundary conditions, they become

$$\begin{cases} \xi_z(0) = 0 \\ \lim\limits_{s\to\infty} \xi_z(s) = \xi_z^{(o)} = 2\kappa \end{cases} \tag{13}$$

Having identified a second-order PDE with sufficient auxiliary conditions, partial integration may be pursued to retrieve

$$\xi_z(s) = 2\kappa\left[1 - \exp\left(-\frac{1}{2}\alpha s\right)\right] \tag{14}$$

Rewriting Eq. (14) in terms of the original variables, a viscous-corrected axial velocity is realized. This solution satisfies the no-slip requirement and reproduces the outer solution at a sufficient distance from the sidewall. It is given by

$$\begin{aligned} u_z(r,z) &= 2\pi\kappa z\cos(\pi r^2)[1 - e^{-\frac{1}{4}(\frac{1}{6}\pi^2-1)V(1-r^2)}] \\ &= u_z^{(o)}[1 - e^{-\frac{1}{4}(\frac{1}{6}\pi^2-1)V(1-r^2)}] \end{aligned} \tag{15}$$

Here $V = 2\pi\kappa/\varepsilon$ is the vortex Reynolds number discussed by Majdalani and Chiaverini [28]. Equation (15) reflects a similar wall correction to that observed in the tangential direction, specifically,

$$u_\theta = u_\theta^{(o)}[1 - e^{-\frac{1}{4}Vr^2} - e^{-\frac{1}{4}(\frac{1}{6}\pi^2-1)V(1-r^2)}]; \qquad u_\theta^{(o)} = r^{-1} \tag{16}$$

B. Radial Corrections

Some inviscid profiles such as those obtained by Culick [34] or Majdalani and Saad [35] satisfy the no-slip condition at the sidewall by virtue of their orthogonal entry at the injecting surface. The inclusion of viscosity in the treatment of such problems often leads to negligible variations in the original flow configuration. The same may be said of the radial velocity of the bidirectional vortex, especially that it identically vanishes at the sidewall. For such a solution, the role and necessity of a viscous correction may not be known beforehand. To make headway, we proceed by considering the reduced radial momentum equation in which second-order viscous terms are retained. This is done in the interest of consistency with the axial and tangential solutions. The radial analysis begins with

$$\varepsilon\left(\frac{\partial^2 u_r}{\partial r^2} + \frac{1}{r}\frac{\partial u_r}{\partial r} - \frac{u_r}{r^2}\right) - u_r\frac{\partial u_r}{\partial r} + \frac{u_\theta^2}{r} - u_z\frac{\partial u_r}{\partial z} = \frac{\partial p}{\partial r} \tag{17}$$

where

$$\begin{cases} u_r(1) = 0 & \text{no slip} \\ \lim\limits_{r\to 0} u_r(r) = u_r^{(o)} & \text{merging with outer solution} \end{cases} \tag{18}$$

Here $u_r^{(o)} = -r^{-1}\kappa\sin(\pi r^2)$. The next step is to ignore axial derivatives by insisting that radial effects dominate. In the process, the pressure gradient is calculated from the outer solution obtained by Vyas and Majdalani [24], particularly,

$$\frac{\partial p}{\partial r} = \frac{\kappa^2}{r^3}\sin^2(\pi r^2)[1 - 2\kappa\pi r^3\cot(\pi r^2)] + \frac{u_\theta^2}{r} \tag{19}$$

When Eq. (19) is substituted back into Eq. (17), the u_θ^2/r terms cancel. What remains on the right-hand side may be recognized to be $O(\kappa^2)$ near the wall. Thereafter, the inviscid solution may be injected into the coefficients of the boundary-layer equation. These operations turn Eq. (17) into

$$\varepsilon\left[\frac{1}{r}\frac{\mathrm{d}}{\mathrm{d}r}\left(r\frac{\mathrm{d}u_r}{\mathrm{d}r}\right) + \frac{\kappa}{r^3}\sin(\pi r^2)\right] + \frac{\kappa}{r}\sin(\pi r^2)\frac{\mathrm{d}u_r}{\mathrm{d}r} = O(\kappa^2) \tag{20}$$

The standard transformation $\eta = \pi r^2$ may now be used. It yields

$$\varepsilon\left[\frac{\mathrm{d}^2 u_r}{\mathrm{d}\eta^2} + \frac{1}{\eta}\frac{\mathrm{d}u_r}{\mathrm{d}\eta} + \frac{\kappa\sqrt{\pi}}{4\eta^{5/2}}\sin(\eta)\right] + \frac{\kappa}{2\eta}\sin(\eta)\frac{\mathrm{d}u_r}{\mathrm{d}\eta} = O(\kappa^2) \tag{21}$$

To magnify the region of nonuniformity, stretching of the radial coordinate near the wall is required. Using the slow variable $s = (\pi - \eta)/\delta$, one may substitute into Eq. (21) and expand the sinusoidal terms. One gets

$$\begin{aligned} &\frac{\varepsilon}{\delta^2}\left[\frac{\mathrm{d}^2 u_r}{\mathrm{d}s^2} - \frac{\delta}{\pi - s\delta}\frac{\mathrm{d}u_r}{\mathrm{d}s} + \frac{\delta^2\kappa\sqrt{\pi}}{4(\pi - s\delta)^{5/2}}\sin(\pi - s\delta)\right] \\ &\quad + \frac{\kappa}{2\delta}\left(\frac{\pi^2}{6} - 1\right)\frac{\mathrm{d}u_r}{\mathrm{d}s} = \frac{1}{4\pi(\pi - s\delta)}O(\kappa^2) \end{aligned} \tag{22}$$

where a distinguished limit of $\delta \approx \varepsilon/\kappa$ reemerges. Without loss in generality, we insert $\delta = \varepsilon/\kappa$ into Eq. (22) and drop the terms of higher order. A simple equation ensues, namely,

$$\frac{\mathrm{d}^2 u_r}{\mathrm{d}s^2} + \frac{\alpha}{2}\frac{\mathrm{d}u_r}{\mathrm{d}s} = 0 \quad \text{with} \quad \begin{cases} u_r(0) = 0 \\ \lim\limits_{s\to\infty} u_r(s) = u_r^{(o)} \end{cases} \tag{23}$$

To overcome the difficulty of equating a constant limit to a variable outer solution, we introduce $\xi_r = ru_r/\sin(\pi r^2)$. Subsequent substitution into Eq. (23) leads to

$$\begin{aligned} \frac{\partial u_r}{\partial s} &= \left[\frac{2\pi\cos\varphi}{V\sqrt{1 - 2sV^{-1}}} + \frac{\sin\varphi}{V(1 - 2sV^{-1})^{3/2}}\right]\xi_r \\ &\quad + \frac{\sin\varphi}{\sqrt{1 - 2sV^{-1}}}\frac{\partial\xi_r}{\partial s} \simeq \frac{\sin\varphi}{\sqrt{1 - 2sV^{-1}}}\frac{\partial\xi_r}{\partial s}; \varphi \equiv 2\pi sV^{-1} \end{aligned} \tag{24}$$

$$\begin{aligned} \frac{\partial^2 u_r}{\partial s^2} &= \left[\frac{4\pi\cos\varphi}{V^2(1 - 2sV^{-1})^{3/2}} + \frac{3\sin\varphi}{V^2(1 - 2sV^{-1})^{5/2}}\right. \\ &\quad \left. - \frac{4\pi^2\sin\varphi}{V^2\sqrt{1 - 2sV^{-1}}}\right]\xi_r + 2\left[\frac{2\pi\cos\varphi}{V\sqrt{1 - 2sV^{-1}}}\right. \\ &\quad \left. + \frac{\sin\varphi}{V(1 - 2sV^{-1})^{3/2}}\right]\frac{\partial\xi_r}{\partial s} + \frac{\sin\varphi}{\sqrt{1 - 2sV^{-1}}}\frac{\partial^2\xi_r}{\partial s^2} \\ &\simeq \frac{\sin\varphi}{\sqrt{1 - 2sV^{-1}}}\frac{\partial^2\xi_r}{\partial s^2} \end{aligned} \tag{25}$$

These derivatives change Eq. (23) into

$$\frac{\mathrm{d}^2\xi_r}{\mathrm{d}s^2} + \frac{\alpha}{2}\frac{\mathrm{d}\xi_r}{\mathrm{d}s} = 0 \quad \text{with} \quad \begin{cases} \xi_r(0) = 0 \\ \lim\limits_{s\to\infty}\xi_r(s) = -\kappa \end{cases} \tag{26}$$

Forthwith, a solution may be achieved in terms of

$$\xi_r(s) = -\kappa[1 - \exp(-\tfrac{1}{2}\alpha s)] \tag{27}$$

or, in terms of original variables, we extract

$$\begin{aligned} u_r(r,z) &= -\tfrac{\kappa}{r}\sin(\pi r^2)[1 - e^{-\frac{1}{4}(\frac{1}{6}\pi^2-1)V(1-r^2)}] \\ &= u_r^{(o)}[1 - e^{-\frac{1}{4}(\frac{1}{6}\pi^2-1)V(1-r^2)}] \end{aligned} \tag{28}$$

Note that the viscous correction multiplier on the right-hand-side of Eq. (28) has the same form as that affecting the axial velocity.

III. Results and Discussion

A. Improved Velocity Profiles

The modified axial velocity captures the effects of fluid friction near the wall. It rectifies the deficiency in the inviscid solution by permitting the satisfaction of the no-slip condition. Figure 4 illustrates the behavior of the present solution with respect to two key parameters: position and vortex Reynolds number. Because the original solution was linearly dependent on the axial coordinate, we continue to observe larger axial velocities at progressively larger axial distances. As in the case of the tangential velocity, we recognize

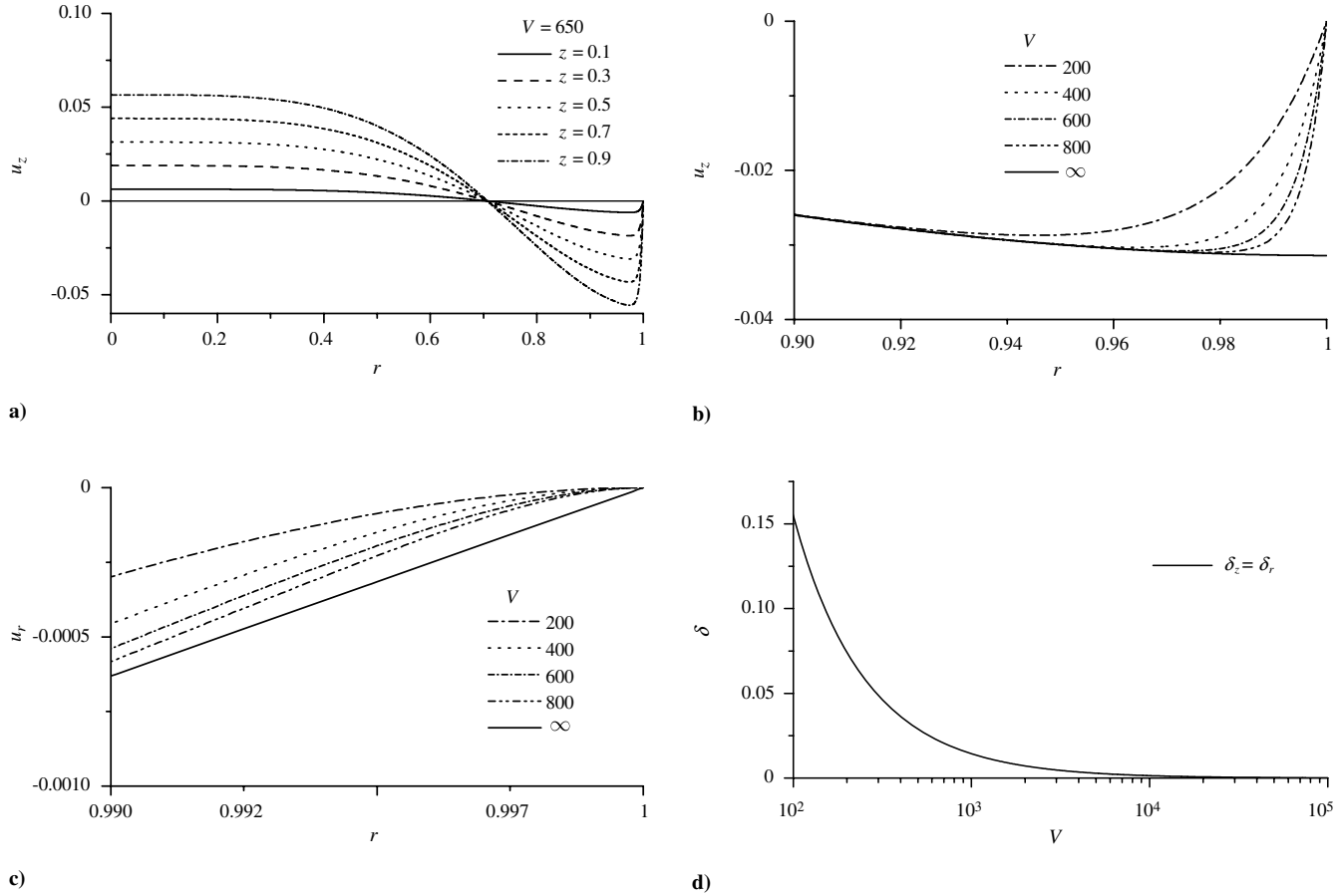

Fig. 4 Effects of wall friction: a) axial velocity component at several axial positions and $V = 650$, b) magnified sidewall region for better depiction of axial boundary-layer behavior at $z = 0.5$, c) radial velocity profile shown near the sidewall at several values of V, and d) boundary-layer thicknesses as a function of V.

a strong dependence on the vortex Reynolds number, a dimensionless group that combines the viscous Reynolds number, swirl number, and the chamber aspect ratio. On the one hand, in the limiting case of $V \to 0$, the absence of a mean inflow velocity causes the solution to categorically vanish. On the other hand, we can see from Fig. 4b that, as the vortex Reynolds number increases, the viscous layer narrows, and the solution shifts toward its inviscid form. Mathematically, this observation can be confirmed by setting $V \to \infty$ in Eq. (15).

Our hypothesis is confirmed in Fig. 4c, in which the inviscid solution is gradually regained at a relatively small distance from the wall. Of course, this observation correlates well with the idea that viscous effects are secondary in nature. Note that, as the vortex Reynolds number increases, the inviscid solution becomes nearly valid over the entire domain. Viscous effects are seen to promote smoothing of u_r, causing both the velocity and its derivative to vanish at the wall. This behavior has a direct bearing on the shear stresses and, consequently, on the potential for roll torques.

B. Axial and Radial Boundary Layers

A closed-form expression can be derived for the boundary-layer thickness by stating that the boundary layer, δ, is the distance required for the viscous solution to reach 99% of its outer, inviscid form. As one would expect, it leads to explicit solutions that are dependent on the vortex Reynolds number. Thus, after locating the radial position corresponding to the edge of the wall layer, this distance may be subtracted from the radius of the chamber to deduce the actual boundary-layer thickness. Given that both profiles exhibit the same viscous correction, a simple boundary-layer thickness may be determined that is identical to the tangential wall boundary-layer thickness, δ_w, obtained in [28]. In summary, we have

$$\delta_z = \delta_r = \delta_w = 1 - \sqrt{1 + \frac{4\,\ell n(0.01)}{\alpha V}} \simeq 1 - \sqrt{1 - \frac{28.562}{V}} \approx \frac{14.281}{V}\left(1 + \frac{7.1405}{V} + \cdots\right) \tag{29}$$

A one-term approximation in Eq. (29) will accrue an error of less than 1% when $V > 722$. Figure 4d shows the effect of increasing the vortex Reynolds number. Clearly, as V increases, the boundary-layer thickness diminishes. Eventually, as confirmed through Eq. (29), the thickness becomes inversely proportional to V. Then as $(\delta_z, \delta_r) \to 0$, the inviscid solution is recovered.

To verify our scaling analysis, we choose to generate values for κ and ε and compare the calculated boundary-layer thickness to the thickness granted by the distinguished limit. With values of $\kappa = 10^{-2}$ and $\varepsilon = 10^{-4}$, the calculated vortex Reynolds number is found to be 628, with a thickness of $\delta_z = 0.0230$. The distinguished limit predicts $\delta = \varepsilon/\kappa = 0.01$, which is of the same order as the boundary-layer region. Compared to the tangential core and wall boundary layers, δ_c and δ_w [28], we have $\delta_c \simeq 2.24/V^{\frac{1}{2}}$ and $\delta_w = \delta_z = \delta_r$. Therefore, in reference to the core layer, we may put

$$\frac{\delta_z}{\delta_c} = \frac{\delta_r}{\delta_c} = \frac{\delta_w}{\delta_c} \simeq 0.446068\sqrt{V}\left(1 - \sqrt{1 - \frac{28.562}{V}}\right) \approx \frac{6.3703}{\sqrt{V}}\left(1 + \frac{7.1405}{V} + \cdots\right); \qquad V > 49 \tag{30}$$

A comparison between the boundary layers is given in Table 1. At first glance, the equality between the axial and tangential boundary layers may appear paradoxical. The unsuspecting analyst may anticipate a steady Prandtl layer to grow in the streamwise direction.

Table 1 Comparison of axial, radial, core, and tangential boundary layers at several values of V

V	$\delta_z = \delta_r = \delta_w$	δ_c
200	0.07415	0.15852
400	0.03636	0.11209
600	0.02409	0.09152
800	0.01801	0.07926
1000	0.01438	0.07089

However, when recalling that the axial pressure gradient is negligible and that the dominant radial pressure gradient acts uniformly along the length of our short chamber, the constant thickness of the tangential boundary layer is no longer surprising. Mathematically, it can be seen that the boundary-layer equations are similar in both the tangential and axial directions. Specifically, both equations are axially independent and exhibit a distinguished limit that showcases viscous diffusion and radial convection caused by the outflow velocity at the edge of the layer (see Fig. 3). This balance supports the notion that both boundary layers are axially invariant and appear at the same order.

In hindsight, an alternate physical explanation may be offered. By rethinking this problem, the requirement for the axial boundary layer to match its tangential counterpart could have been deduced from physical arguments alone, without the need for analysis. The reason is this: In view of the tangential boundary layer being axially invariant, its thickness δ_w remains constant at any position inside the chamber. This feature is illustrated in Fig. 5, in which several circular strips, representing the envelope of δ_w, are graphically displayed at three axial stations. It follows that the thickness of the envelope in the longitudinal direction (thin dashed lines representing δ_z in Fig. 5) must also remain constant to prevent an axial increase in δ_w. However, because of boundary-layer orthogonality, any increase in δ_z cannot be realized without affecting the size of δ_w. These observations confirm the consistency of the asymptotic treatment, as any other outcome would have constituted a violation of the basic assumptions underlying the bidirectional vortex model.

It may be helpful to note another perspective on this problem that may be gained from examining the resultant velocity and its impact on the flow motion. Given that fluid particles only sense the resultant velocity $\boldsymbol{u}$ (i.e., the individual components $(\boldsymbol{u}_r, \boldsymbol{u}_\theta, \boldsymbol{u}_z)$ are mere orthogonal projections), it may be safely argued that the resultant boundary layer is directly controlled by $\boldsymbol{u}$. At the outset, the composite layer is seen to be dominated by the swirl velocity, given that $\boldsymbol{u} = \boldsymbol{u}_\theta + O(\kappa)$ The actual boundary layer forming above the surface, which is the by-product of the axial and tangential layers, must therefore conform to the flow being vortex driven. It thus comprises a spiraling axisymmetric layer that ascends the chamber vertically without experiencing any significant growth or depreciation.

C. Shear-Stress Tensor

The shear stress may be evaluated to help in determining the force exerted by the fluid on the sidewall, in addition to the ensuing roll torque. Based on standard relations, one may first calculate the stresses acting on the fluid using

$$\begin{aligned}\tau_{rr} &= 2\varepsilon\frac{\partial u_r}{\partial r} = \varepsilon^2 V\left\{\frac{\sin(\pi r^2)}{\pi r^2}[1-e^{-\frac{1}{4}\alpha V(1-r^2)}]\right.\\ &\left.+\frac{\alpha}{\pi}V\sin(\pi r^2)e^{-\frac{1}{4}\alpha V(1-r^2)} - 2\cos(\pi r^2)[1-e^{-\frac{1}{4}\alpha V(1-r^2)}]\right\}\\ &= 2\pi\varepsilon\kappa\left\{\frac{\alpha}{\pi}V\sin(\pi r^2)e^{-\frac{1}{4}\alpha V(1-r^2)}\right.\\ &\left.+\left[\frac{\sin(\pi r^2)}{\pi r^2} - 2\cos(\pi r^2)\right][1-e^{-\frac{1}{4}\alpha V(1-r^2)}]\right\} \qquad (31)\end{aligned}$$

$$\begin{aligned}\tau_{\theta\theta} &= 2\varepsilon\left(\frac{1}{r}\frac{\partial u_\theta}{\partial\theta}+\frac{u_r}{r}\right) = -\frac{\varepsilon^2 V}{\pi r^2}\sin(\pi r^2)[1-e^{-\frac{1}{4}\alpha V(1-r^2)}]\\ &= -\frac{2\varepsilon\kappa}{r^2}\sin(\pi r^2)[1-e^{-\frac{1}{4}\alpha V(1-r^2)}] \qquad (32)\end{aligned}$$

$$\begin{aligned}\tau_{zz} &= 2\varepsilon\frac{\partial u_z}{\partial z} = 2\varepsilon^2 V\cos(\pi r^2)[1-e^{-\frac{1}{4}\alpha V(1-r^2)}]\\ &= 4\pi\varepsilon\kappa\cos(\pi r^2)[1-e^{-\frac{1}{4}\alpha V(1-r^2)}] \qquad (33)\end{aligned}$$

$$\begin{aligned}\tau_{r\theta} &= \varepsilon\left[\frac{1}{r}\frac{\partial u_r}{\partial\theta}+r\frac{\partial}{\partial r}\left(\frac{u_\theta}{r}\right)\right] = \frac{\varepsilon}{2r^2}\left[\frac{(4+r^2V)e^{-\frac{1}{4}Vr^2}}{1-e^{-\frac{1}{4}V}}\right.\\ &\left.+\frac{[4-r^2V(\frac{1}{6}\pi^2-1)]e^{-\frac{1}{4}\alpha V(1-r^2)}-2-2e^{-\frac{1}{4}\alpha V}}{1-e^{-\frac{1}{4}\alpha V}} - 2\coth\left(\frac{V}{8}\right)\right]\\ &\simeq \frac{\varepsilon}{2r^2}[(4+Vr^2)e^{-\frac{1}{4}Vr^2}+(4-\alpha Vr^2)e^{-\frac{1}{4}\alpha V(1-r^2)}-4]\\ &\text{(with no transcendental parts)} \qquad (34)\end{aligned}$$

$$\tau_{\theta z} = \varepsilon\left(\frac{1}{r}\frac{\partial u_z}{\partial\theta}+\frac{\partial u_\theta}{\partial z}\right) = 0 \qquad (35)$$

and

$$\begin{aligned}\tau_{zr} &= \varepsilon\left(\frac{\partial u_z}{\partial r}+\frac{\partial u_r}{\partial z}\right) = \varepsilon\frac{\partial u_z}{\partial r} = -\frac{1}{2}\varepsilon^2 Vrz\{4\pi\sin(\pi r^2)\\ &\times[1-e^{-\frac{1}{4}\alpha V(1-r^2)}]+\alpha V\cos(\pi r^2)e^{-\frac{1}{4}\alpha V(1-r^2)}\}\\ &= -\pi\varepsilon\kappa rz\{4\pi\sin(\pi r^2)[1-e^{-\frac{1}{4}\alpha V(1-r^2)}]\\ &+\alpha V\cos(\pi r^2)e^{-\frac{1}{4}\alpha V(1-r^2)}\} \qquad (36)\end{aligned}$$

These are illustrated in Fig. 6. Having fully determined the shear-stress tensor, it is possible to evaluate its resultant at the sidewall. This enables us to predict the roll torques in the vortex chamber by integrating the shear stress over the sidewall. By calculating each member in Eqs. (31–36) as $r \to 1$, we collect

$$\begin{cases}\tau_{rr}^{(w)} = \tau_{\theta\theta}^{(w)} = \tau_{zz}^{(w)} = \tau_{\theta z}^{(w)} = 0\\ \tau_{r\theta}^{(w)} = -\frac{1}{2}\alpha\varepsilon V = -\pi(\frac{1}{6}\pi^2-1)\kappa\\ \tau_{zr}^{(w)} = \frac{1}{2}\alpha\varepsilon^2V^2z = 2(\frac{1}{6}\pi^2-1)\pi^2\kappa^2z\end{cases} \qquad (37)$$

Compared to the results in [28], the added corrections slightly alter the shear-stress estimation at the wall. With the viscous amendments introduced here, τ_{zz} and τ_{rr} are found to be identically zero, whereas τ_{zr} appears to have a small finite value. A comparison of these results to those of the inviscid solution is given in Table 2. Using a Pythagorean sum of orthogonal components, the total shear stress may be calculated from

$$\tau_0^{(w)} = \sqrt{[\tau_{r\theta}^{(w)}]^2+[\tau_{zr}^{(w)}]^2} = \tfrac{1}{2}\alpha\varepsilon V\sqrt{1+\varepsilon^2V^2z^2} \qquad (38)$$

This resultant total stress considers shearing forces contributing to pitch and roll. Although stresses contributing to pitch cancel due to axisymmetry, those affecting roll do not.

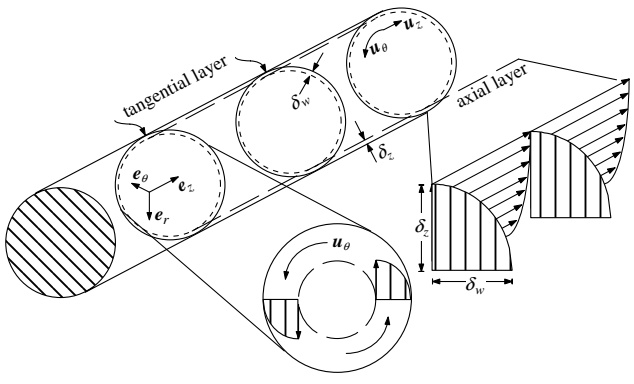

Fig. 5 Axial invariance of the tangential and axial boundary layers.

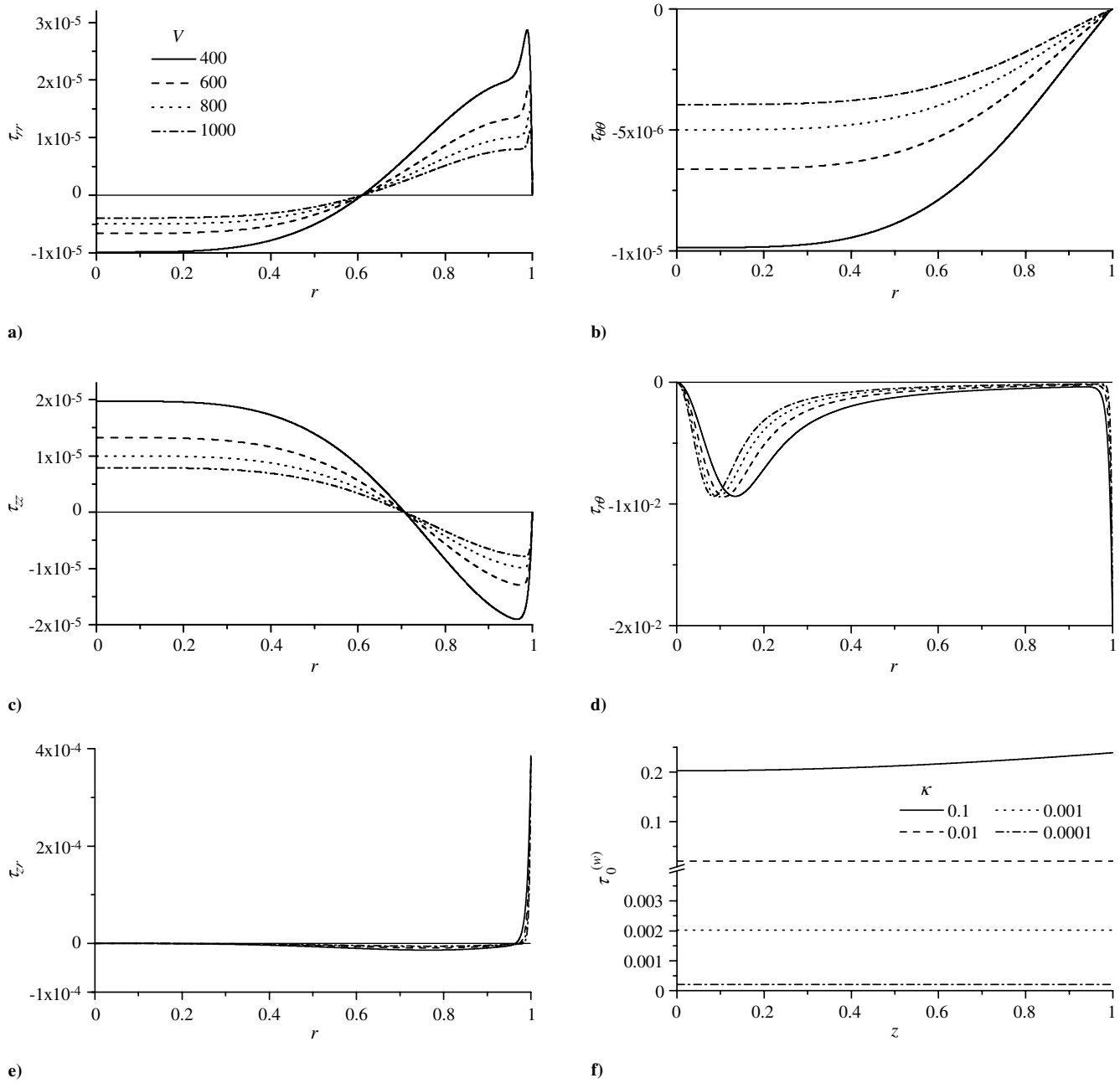

Fig. 6 Shear stresses at several values of V, $z = 0.3$, and $\kappa = 0.01$: a) τ_{rr}, b) $\tau_{\theta\theta}$, c) τ_{zz}, d) $\tau_{r\theta}$, e) τ_{zr}, and f) $\tau_0^{(w)}$, where κ is varied by three orders of magnitude as indicated.

By carefully examining Figs. 6a–6f, it may be seen that the flow is still dominated by the shear component $\tau_{r\theta}$, which remains an order of magnitude larger than τ_{zr}. The roll torque can be determined by first integrating the azimuthal shear stress at the wall, $\tau_{r\theta}^{(w)}$, over the lateral surface of the chamber to determine the tangential force. One gets

$$F_\theta^{(w)} = \int_0^{2\pi}\int_0^l \frac{1}{2}\alpha\varepsilon V \,\mathrm{d}z\,\mathrm{d}\theta = \pi\alpha\varepsilon V l = Q_i\pi\alpha \tag{39}$$

Note that $-\tau_{r\theta}^{(w)}$ is used to obtain the stress exerted by the fluid on the wall. Thus, given a chamber of unit radius, the dimensionless tangential shear force acting on the inner wall matches the roll torque T_θ acting on the same surface. When written in dimensional form, the torque may be expressed as

$$\begin{aligned}\bar{T}_\theta &= \pi\alpha Q_i\rho U^2 a^3 = (\tfrac{1}{6}\pi^3 - \pi)\rho\bar{Q}_i U a\\ &= 2.02612\dot{m}_i U a = 1.01306\dot{m}_i U D;\\ D &= 2a\end{aligned} \tag{40}$$

Note that the torque exerted by the fluid on the wall acts in the same direction as the tangential velocity at entry. It is directly proportional to the mass flow rate $\dot{m}_i$, circumferential injection velocity U, and chamber diameter D. Recalling that $\bar{F}_M = \dot{m}_i U$ represents the fluid momentum force according to control-volume theory, the actual torque is nearly equal to the injection moment couple, namely, the product of $\bar{F}_M$ and the chamber diameter D. The small discrepancy of 1.3% between the differential and integral (control-volume) analyses may be attributed to two sources. The first is connected with the asymptotic approximations entailed in the analysis (such as the

Table 2 Comparison of the inviscid and viscous shear-stress components evaluated at the sidewall

Wall shear stresses	With no axial/radial boundary layers	With tridirectional boundary layers
$\tau_{rr}^{(w)}$	$2\varepsilon^2 V$	0
$\tau_{\theta\theta}^{(w)}$	0	0
$\tau_{zz}^{(w)}$	$-2\varepsilon^2 V$	0
$\tau_{r\theta}^{(w)}$	$-\pi\alpha\kappa$	$-\pi\alpha\kappa$
$\tau_{\theta z}^{(w)}$	0	0
$\tau_{zr}^{(w)}$	0	$2\alpha\pi^2\kappa^2 z$

evaluation of α), and the second may be ascribed to the use of U, both as the average tangential velocity in the control-volume analysis based on an average mass flow rate $\dot{m}_i$ and as the maximum velocity at entry in the differential analysis.

D. Pressure Distribution

The pressure is evaluated with the viscous corrections at hand. Based on Euler's equations, we obtain a leading-order solution from

$$\frac{\partial p}{\partial r} = \frac{u_\theta^2}{r} - u_r\frac{\partial u_r}{\partial r} - u_z\frac{\partial u_r}{\partial z} \tag{41}$$

Injecting the improved representations for the velocity components, we retrieve

$$\begin{aligned}\frac{\partial p}{\partial r} &= \kappa^2 r^{-1}\sin(\pi r^2)[1-e^{-\frac{1}{4}\alpha V(1-r^2)}]\\ &\times\left\{[r^{-2}\sin(\pi r^2)-2\pi\cos(\pi r^2)][1-e^{-\frac{1}{4}\alpha V(1-r^2)}]\right.\\ &\left.+\frac{1}{2}\alpha V\sin(\pi r^2)e^{-\frac{1}{4}\alpha V(1-r^2)}\right\}+\frac{1}{r^3}\left[\frac{1-e^{-\frac{1}{4}Vr^2}}{1-e^{-\frac{1}{4}V}}\right.\\ &\left.+\frac{1-e^{-\frac{1}{4}\alpha V(1-r^2)}}{1-e^{-\frac{1}{4}\alpha V}}-1\right]^2\end{aligned} \tag{42}$$

Equation (42) may be carefully simplified and collapsed into

$$\frac{\partial p}{\partial r} \simeq \frac{1}{r^3}[1-e^{-\frac{1}{4}Vr^2}-e^{-\frac{1}{4}\alpha V(1-r^2)}]^2 \tag{43}$$

As for the axial gradient, it can be similarly obtained from

$$\frac{\partial p}{\partial z} = -u_r\frac{\partial u_z}{\partial r} - u_z\frac{\partial u_z}{\partial z} \tag{44}$$

At the onset of this calculation, it may be realized that the axial gradient is of order κ^2. One may also recall that radial terms of order κ^2 have been discounted elsewhere. To remain asymptotically consistent with the truncation order incurred in this model, the axial gradient is hereby dismissed. It may be easily shown that its retention is immaterial. Moreover, we are now able to retrieve the pressure field from Eq. (43).

With the help of symbolic software [36], Eq. (43) may be integrated and anchored to a constant reference pressure at the wall, $p_0 = p(1)$. The result is

$$\begin{aligned}p &= p_0 - \frac{1}{2r^2}\{(1-e^{-\frac{1}{4}Vr^2})^2+[1-e^{-\frac{1}{4}\alpha V(1-r^2)}]^2\\ &-1+2e^{-\frac{1}{4}V[\alpha+(1-\alpha)r^2]}\}-\frac{1}{4}V\left\{\mathrm{Ei}\left(-\frac{1}{2}Vr^2\right)\right.\\ &-\mathrm{Ei}\left(-\frac{1}{4}Vr^2\right)+\alpha e^{-\frac{1}{4}\alpha V}\left[\mathrm{Ei}\left(\frac{1}{4}\alpha Vr^2\right)-\mathrm{Ei}\left(\frac{1}{4}\alpha V\right)\right]\\ &\left.-\alpha e^{-\frac{1}{2}\alpha V}\left[\mathrm{Ei}\left(\frac{1}{2}\alpha Vr^2\right)-\mathrm{Ei}\left(\frac{1}{2}\alpha V\right)\right]\right\}\end{aligned} \tag{45}$$

where $\mathrm{Ei}(x)$ denotes the second exponential integral function,

$$\mathrm{Ei}(x) = \gamma + \ell_n|x| + \sum_{m=1}^{\infty}\frac{x^m}{m!m};$$

$$\gamma \simeq 0.5772156649 \qquad \text{(Euler's constant)} \tag{46}$$

Note that when Eq. (45) is compared to its precursor in [28], an additional term appears that may be attributed to the influence of the axial boundary layer. This term is $-r^{-2}\exp\{-\frac{1}{4}V[\alpha+(1-\alpha)r^2]\}$. Nonetheless, when the pressure is plotted in Fig. 7, the influence of this term is found to be small. We deduce that the axial and radial corrections for the pressure are minor.

E. Vorticity and Circulation

1. Vorticity

The axisymmetric vorticity is given by

$$\begin{aligned}\boldsymbol{\Omega} &= -\frac{\partial u_\theta}{\partial z}\boldsymbol{e}_r+\left(\frac{\partial u_r}{\partial z}-\frac{\partial u_z}{\partial r}\right)\boldsymbol{e}_\theta+\left(\frac{\partial u_\theta}{\partial r}+\frac{u_\theta}{r}\right)\boldsymbol{e}_z\\ &= \pi r z\kappa\{\alpha V e^{-\frac{1}{4}\alpha V(1-r^2)}\cos(\pi r^2)\\ &+4\pi[1-e^{-\frac{1}{4}\alpha V(1-r^2)}]\sin(\pi r^2)\}\boldsymbol{e}_\theta\\ &+\frac{V}{2}\left[\frac{e^{-\frac{1}{4}Vr^2}}{1-e^{-\frac{1}{4}V}}-\frac{\alpha e^{-\frac{1}{4}\alpha V(1-r^2)}}{1-e^{-\frac{1}{4}\alpha V}}\right]\boldsymbol{e}_z\end{aligned} \tag{47}$$

In the Rankine vortex [1], a piecewise solution is posited in which the rotational core is governed by solid-body rotation, and the irrotational tail is derivable from a scalar potential. Obviously, no vorticity can originate from the tail, especially in an unbounded domain. In the confined bidirectional vortex, a section of the free vortex segment resembles that of Rankine's and remains, as such, vorticity free. Axial vorticity is only recovered in the vicinity of the

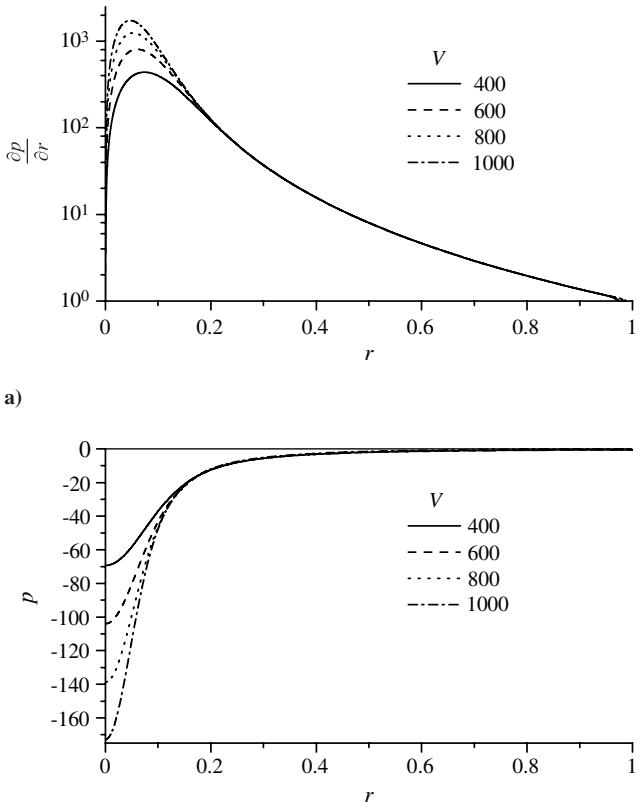

Fig. 7 Variation of the radial pressure gradient and pressure at four values of V.

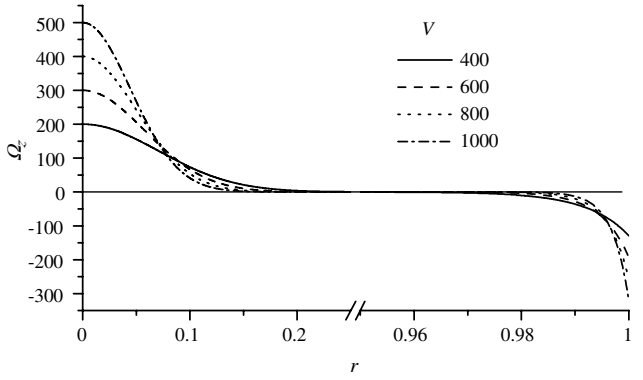

a)

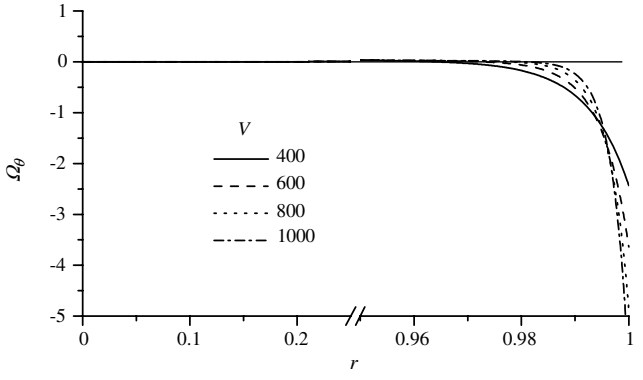

b)

Fig. 8 Sidewall and near-core behavior at four values of V ($\kappa = 0.01$, $z = 3$): a) axial vorticity, and b) tangential vorticity.

wall and core regions as seen in Fig. 8. The expression that we arrive at is identical to that of Majdalani and Chiaverini [28], particularly,

$$\Omega_z \simeq \tfrac{1}{2}V[e^{-\frac{1}{4}Vr^2} - \alpha e^{-\frac{1}{4}\alpha V(1-r^2)}] \tag{48}$$

The tangential vorticity Ω_θ is of order κ and is hence small in comparison to the axial component. This behavior reinforces the character of the flowfield as being fundamentally swirl dominated. However, although the tangential vorticity is approximately zero throughout the majority of the chamber, its contribution becomes appreciable in the sidewall region.

2. Circulation

The circulation Γ can be directly related to the vorticity through Stokes's theorem, namely,

$$\Gamma = \iint_A (\nabla \times \boldsymbol{u}) \cdot \boldsymbol{n}\, \mathrm{d}A \tag{49}$$

In our case, Γ is the axial component of vorticity integrated over the circular cross-sectional area of the chamber A. This operation translates into

$$\Gamma = \frac{1}{2}V \int_0^{2\pi} \int_0^1 \left[\frac{e^{-\frac{1}{4}Vr^2}}{1 - e^{-\frac{1}{4}V}} - \frac{\alpha e^{-\frac{1}{4}\alpha V(1-r^2)}}{1 - e^{-\frac{1}{4}\alpha V}} \right] r\, \mathrm{d}r\, \mathrm{d}\theta = 0 \tag{50}$$

Note that the integral vanishes identically. Upon further scrutiny, one identifies a one-to-one cancellation of the vorticity products in the core region with those in the boundary-layer region. For external flows, as for some of the classical vortex models that exhibit a singularity at the core, a finite circulation is obtained when the singularity is included in the domain of integration [37].

F. Swirling Intensity

As a predictor of mixing potential with respect to various configurations, we evaluate the swirling intensity according to Chang and Dhir [38], and aptly apply it to the bidirectional vortex. We find

$$\tilde{\Omega} = \frac{\int_0^{1/\sqrt{2}} u_z u_\theta r\, \mathrm{d}r}{4(\int_0^{1/\sqrt{2}} u_z r\, \mathrm{d}r)^2} \tag{51}$$

Subsequent symbolic programming may be used to evaluate $\tilde{\Omega}$; we get

$$\tilde{\Omega} = -\frac{\pi\sqrt{\pi}(1-i)}{4\sqrt{2}} \frac{1}{\kappa z} \left\{ \frac{\mathrm{erf}[\frac{1}{4}(1+i)\sqrt{4\pi - iV}]}{\sqrt{4\pi - iV}} + \frac{\mathrm{erfi}[\frac{1}{4}(1+i)\sqrt{4\pi + iV}]}{\sqrt{4\pi + iV}} - \frac{(1+i)}{\sqrt{\pi}} C(1) \right\} \tag{52}$$

which is true for $V > 49$; here $C(1) \simeq 0.779893$, where $C(x)$ is the Fresnel integral defined as

$$C(x) = \int_0^x \cos\left(\frac{1}{2}\pi r^2\right) \mathrm{d}r \tag{53}$$

Equation (52) provides an accurate and compact expression for the swirling intensity. Note that as the vortex Reynolds number becomes very large, the swirling intensity approaches an asymptotic value given by

$$\tilde{\Omega}_\infty \approx \frac{\pi C(1)}{2\sqrt{2}} \frac{1}{\kappa z} = \frac{0.866244}{\kappa z} \tag{54}$$

This can be inferred graphically from Fig. 9. Note that Eq. (52) is identical to the one found by Majdalani and Chiaverini [28]. We

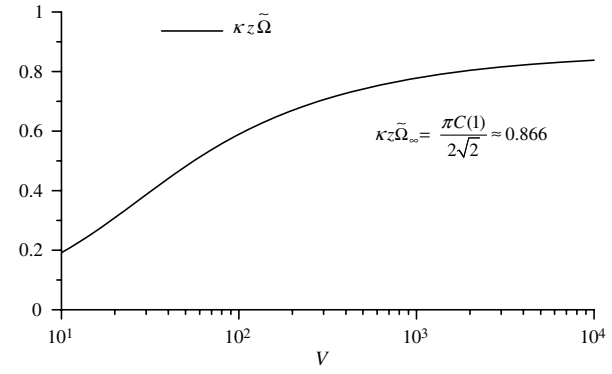

a)

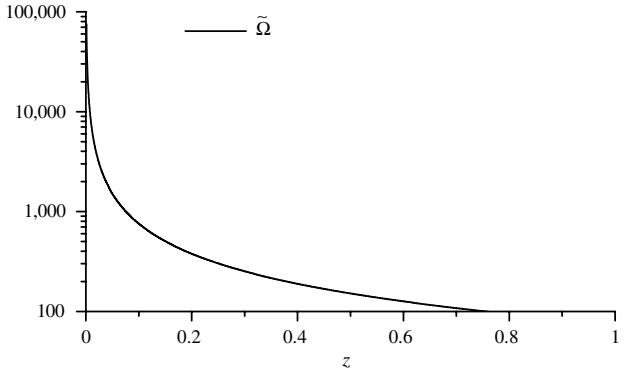

b)

Fig. 9 Variation of swirling intensity: a) vortex Reynolds number, and b) axial distance from the headwall, where $\kappa = 0.01$ and $V = 650$.

conclude that the axial and radial boundary layers have a secondary impact on $\tilde{\Omega}$.

IV. Conclusions

This study extends our analytical treatment of the bidirectional vortex, which is based on solutions obtained from first principles. Both axial and radial boundary layers at the sidewall, which have been dismissed in previous analyses, are accounted for and resolved. Whereas the axial boundary layer is required to bring the parallel component of the velocity to observe the no-slip condition, the radial layer is formed to prevent the abrupt clipping of the radial velocity at the sidewall. The work parallels the analysis of the wall-tangential boundary layer that has resulted in a rectified form of the swirl velocity. Using similar perturbation tools, the theory of matched-asymptotic expansions is applied to capture the small viscous effects at the confining boundary. Additionally, both independent and dependent variables are transformed, lest an intractable problem is obtained. In the tangential direction, a simple boundary condition is imposed on the conserved angular momentum in the far field, namely, a pure constant corresponding to a free vortex, that is, $(ru_\theta) = 1$. Presently, the outer solution corresponds to sinusoidal functions of at least one variable. Thus, after several transformations, expansions, and asymptotic reductions, uniformly valid approximations are derived for both axial and radial velocities. The viscous corrections are found to mirror those constructed in the tangential direction. Their role is to cause the axial velocity to vanish at the sidewall while providing a measure of tempering in the radial profile, causing it to terminate smoothly. We note that, in the process of establishing the inner equations that control the rapid changes in the vicinity of the wall, expressions are obtained that resemble those appropriate for two-dimensional boundary-layer analysis.

The novelty in the present approach stands, perhaps, in the systematic procedure used to reduce the original PDEs into simpler ODEs, followed by leading-order expansions of the coefficients arising in the convective terms. Although classic boundary-layer theory suggests searching for either integral or similarity solutions to the governing equations, neither routes rely on asymptotic matching to produce uniformly valid solutions throughout the domain.

In light of the new corrections, several key characteristics of the bidirectional vortex are quantified. Theoretical thicknesses for the axial and radial layers are extracted, and these are compared to both wall-tangential and core boundary layers. The axial and radial boundary layers are found to be of equal size and consistent with the tangential layer δ_w obtained by Majdalani and Chiaverini [28]. These layers are inversely proportional to the vortex Reynolds number to the extent of increasing with the viscosity, aspect ratio, and swirl number. By the same token, they become thinner with successive increases in the circumferential velocity.

The uniformity observed in the boundary layers, which may be surprising at first, may be physically anticipated without the need for asymptotic analysis. Given that the resultant velocity is nearly equal to the tangential velocity, the boundary-layer thickness is dominated by its tangential component. Moreover, the tangential boundary layer remains invariant in the axial direction to the extent that its thickness measured along the length of the chamber is found to be identical to its thickness measured along the circumference. The equality $\delta_z = \delta_r = \delta_w$ is thus a product of axisymmetry and the invariance of the swirl velocity in the axial direction.

With respect to the shear stresses, the axial and radial corrections help to refine the stress tensor in several of its elements. The $\tau_{zr}^{(w)}$ term and, hence, the total shear are seen to exhibit a small axial dependence that cannot be manifested in the absence of wall friction. We also determine that $\tau_{rr}^{(w)}$ and $\tau_{zz}^{(w)}$ are not asymptotically small but strictly zero. Overall, only secondary contributions to the resultant shear force are realized. With the roll torque being driven by the tangential component, its dimensional form is found to depend on the fluid moment couple, a product of the mass flow rate into the chamber, the circumferential velocity, and the chamber diameter.

When evaluating the pressure gradient, it may be remarked that the prevalent terms are those connected with the swirl velocity. Physically, terms referring to axial and radial velocities or their derivatives are negligible as they tend to be of order κ^2. At length, we recover nearly the same asymptotic form derived by Majdalani and Chiaverini [28]. As for the axial pressure gradient, we find all of its terms to be of order κ^2. In the spirit of asymptotic consistency, the axial pressure dependence is ignored. Qualitatively, a much lower pressure is captured throughout the core in comparison to the wall region. This suction pressure is responsible for attracting the flow inwardly, causing the fluid in the outer annular vortex to negotiate a 180 deg turn at the headwall before reentering the inner vortex. It is also responsible, in part, for the constant crossflow that persists along the length of the mantle, causing the annular fluid to leak inwardly while traversing the chamber height.

With respect to vorticity, the parallelism with the Rankine vortex continues to hold to some extent. Here, too, vorticity is confined to either the viscous core or the sidewall region. We also continue to see vorticity dominated by its axial component and, along with other essential flow features, to be strongly dependent on V. Interestingly, circulation in the presence of bidirectional motion is found to be self-cancelling. This behavior may be attributed to the complex lamellar nature of the base flow. It is also due to a counterbalance between vorticities produced in the core and in the sidewall regions. Despite their presence at the far ends of the domain, their contributions simply cancel. This result prevents us from expressing the bidirectional vortex in terms of circulation. For the same reason, direct correlations with historical models defined by this parameter do not seem possible.

The swirling intensity continues to be largest near the headwall and mostly dominated by the tangential velocity (Fig. 9). The large swirling intensities encountered near the headwall turn this region into an ideal site for mixing. Such behavior is advantageous to the VCCWC chamber, in which the useful attributes of a cyclone are exploited. By exhibiting an internal flowfield that promotes improved mixing between oxidizer and fuel streams, the VCCWC is projected to achieve high efficiency and low-cost operability.

Continued research is projected for the vortex engine. One topic of significant interest is the qualification of the inherent cooling properties of the VCCWC. In this vein, a characterization of the sidewall boundary layers is necessary to resolve the thermal layers. Another topic of interest concerns the daunting task of capturing the Ekman-layerlike boundary layers at the headwall. This is needed to quantify the axial dependence of the tangential velocity near the headwall and remove the singular behavior of the swirl intensity. Other related topics include determining the hydrodynamic and acoustic stability of the bidirectional vortex, the effect of particle entrainment, and the flow analog arising in the context of a hybrid vortex engine for which sidewall injection is considered.

Acknowledgments

The authors are deeply grateful for the support received from the National Science Foundation through grant no. CMMI-0928762. We also thank Martin J. Chiaverini of Orbital Technologies Corporation for contributions provided over the course of this project.

References

[1] Rankine, W. J. M., *A Manual of Applied Mechanics*, 9th ed., C. Griffin and Co., London, 1858.

[2] Lamb, H., *Hydrodynamics*, 6th ed., Cambridge Univ. Press, Cambridge, England, UK, 1932.

[3] Oseen, C., "Uber Wirbelbewegung in einer reibenden Flüssigkeit," *Arkiv för matematik, astronomi och fysik*, Vol. 7, 1912, pp. 14

[4] Burgers, J. M., "A Mathematical Model Illustrating the Theory of Turbulence," *Advances in Applied Mechanics*, Vol. 1, 1948, pp. 171–196.
doi:10.1016/S0065-2156(08)70100-5

[5] Rott, N., "On the Viscous Core of a Line Vortex," *Zeitschrift für Angewandte Mathematik und Physik*, Vol. 9, 1958, pp. 543–553.
doi:10.1007/BF02424773

[6] Batchelor, G. K., "Axial Flow in Trailing Line Vortices," *Journal of Fluid Mechanics*, Vol. 20, No. 4, 1964, pp. 645–658.
doi:10.1017/S0022112064001446

[7] Penner, S. S., "Elementary Considerations of the Fluid Mechanics of Tornadoes and Hurricanes," *Acta Astronautica*, Vol. 17, 1972, pp. 351–362.
[8] Königl, A., "Stellar and Galactic Jets: Theoretical Issues," *Canadian Journal of Physics*, Vol. 64, 1986, pp. 362–368.
[9] Kyrala, A., "An Explanation of the Persistence of the Great Red Spot of Jupiter," *The Moon and the Planets*, Vol. 26, No. 1, 1982, pp. 105–107. doi:10.1007/BF00941374
[10] Eloy, C., and Le Dizès, S., "Three-Dimensional Instability of Burgers and Lamb–Oseen Vortices in a Strain Field," *Journal of Fluid Mechanics*, Vol. 378, No. 1, 1999, pp. 145–166. doi:10.1017/S0022112098003103
[11] Batterson, J. W., Maicke, B. A., and Majdalani, J., "Advancements in Theoretical Models of Confined Vortex Fowfields," JANNAF Paper TP-2007-222, May 2007.
[12] Alekseenko, S. V., Kuibin, P. A., Okulov, V. L., and Shtork, S. I., "Helical Vortices in Swirl Flow," *Journal of Fluid Mechanics*, Vol. 382, No. 1, 1999, pp. 195–243. doi:10.1017/S0022112098003772
[13] Schmid, P. J., and Rossi, M., "Three-Dimensional Stability of a Burgers Vortex," *Journal of Fluid Mechanics*, Vol. 500, No. 1, 2004, pp. 103–112. doi:10.1017/S0022112003007341
[14] Olendraru, C., and Sellier, A., "Viscous Effects in the Absolute–Convective Instability of the Batchelor Vortex," *Journal of Fluid Mechanics*, Vol. 459, No. 1, 2002, pp. 371–396. doi:10.1017/S0022112002008029
[15] Pérez-Saborid, M., Herrada, M. A., Gómez-Barea, A., and Barrero, A., "Downstream Evolution of Unconfined Vortices: Mechanical and Thermal Aspects," *Journal of Fluid Mechanics*, Vol. 471, No. 1, 2002, pp. 51–70. doi:10.1017/S0022112002002021
[16] Sullivan, R. D., "A Two-Cell Vortex Solution of the Navier–Stokes Equations," *Journal of the Aerospace Sciences*, Vol. 26, 1959, pp. 767–768.
[17] Vatistas, G. H., Lin, S., and Kwok, C. K., "Theoretical and Experimental Studies on Vortex Chamber Flows," *AIAA Journal*, Vol. 24, No. 4, 1986, pp. 635–642. doi:10.2514/3.9319
[18] Vatistas, G. H., Lin, S., and Kwok, C. K., "Reverse Flow Radius in Vortex Chambers," *AIAA Journal*, Vol. 24, No. 11, 1986, pp. 1872–1873. doi:10.2514/3.9539
[19] Vatistas, G. H., Jawarneh, A. M., and Hong, H., "Flow Characteristics in a Vortex Chamber," *Canadian Journal of Chemical Engineering*, Vol. 83, No. 6, 2005, pp. 425–436. doi:10.1002/cjce.5450830305
[20] Bloor, M. I. G., and Ingham, D. B., "The Flow in Industrial Cyclones," *Journal of Fluid Mechanics*, Vol. 178, No. 1, 1987, pp. 507–519. doi:10.1017/S0022112087001344
[21] Chiaverini, M. J., Malecki, M. J., Sauer, J. A., and Knuth, W. H., "Vortex Combustion Chamber Development for Future Liquid Rocket Engine Applications," AIAA Paper 2002-2149, July 2002.
[22] Chiaverini, M. J., Malecki, M. J., Sauer, J. A., Knuth, W. H., and Majdalani, J., "Vortex Thrust Chamber Testing and Analysis for O2-H2 Propulsion Applications," AIAA Paper 2003-4473, July 2003.
[23] Chiaverini, M. J., Malecki, M. M., Sauer, J. A., Knuth, W. H., and Hall, C. D., "Testing and Evaluation of Vortex Combustion Chamber for Liquid Rocket Engines," JANNAF TP-2002-0372April 2002.
[24] Vyas, A. B., and Majdalani, J., "Exact Solution of the Bidirectional Vortex," *AIAA Journal*, Vol. 44, No. 10, 2006, pp. 2208–2216. doi:10.2514/1.14872
[25] Majdalani, J., and Rienstra, S. W., "On the Bidirectional Vortex and Other Similarity Solutions in Spherical Coordinates," *Journal of Applied Mathematics and Physics*, Vol. 58, No. 2, 2007, pp. 289–308. doi:10.1007/s00033-006-5058-y
[26] Barber, T. A., and Majdalani, J., "Exact Eulerian Solution of the Conical Bidirectional Vortex," AIAA Paper 2009-5306, Aug. 2009.
[27] Majdalani, J., "Exact Eulerian Solutions of the Cylindrical Bidirectional Vortex," AIAA Paper 2009-5307, Aug. 2009.
[28] Majdalani, J., and Chiaverini, M. J., "On Steady Rotational Cyclonic Flows: The Viscous Bidirectional Vortex," *Physics of Fluids*, Vol. 21, No. 10, 2008, 103603. doi:10.1063/1.3247186
[29] Burgers, J. M., "On the Resistance of Fluids and Vortex Motion," *Proceedings of the Koninklijke Nederlandse Akademie van Wetenschappen*, Vol. 23, No. 1, 1921, pp. 774–782.
[30] Prandtl, L., "Zur Berechnung Der Grenzschichten," *Journal of Applied Mathematics and Mechanics*, Vol. 18, 1938, pp. 77–82.
[31] Conlisk, A. T., "Source-Sink Flows in a Rapidly Rotating Annulus," Ph.D. Dissertation, Purdue Univ., West Lafayette, IN, 1978.
[32] Tetervin, N., "Boundary-Layer Momentum Equations for Three-Dimensional Flow," National Advisory Committee for Aeronautics, NACA TN-1479, Langley Field, VA, Oct. 1947.
[33] Balachandar, S., Buckmaster, J. D., and Short, M., "The Generation of Axial Vorticity in Solid-Propellant Rocket-Motor Flows," *Journal of Fluid Mechanics*, Vol. 429, No. 1, 2001, pp. 283–305. doi:10.1017/S0022112000002688
[34] Culick, F. E. C., "Rotational Axisymmetric Mean Flow and Damping of Acoustic Waves in a Solid Propellant Rocket," *AIAA Journal*, Vol. 4, No. 8, 1966, pp. 1462–1464. doi:10.2514/3.3709
[35] Majdalani, J., and Saad, T., "The Taylor–Culick Profile with Arbitrary Headwall Injection," *Physics of Fluids*, Vol. 19, No. 9, 2007, 093601. doi:10.1063/1.2746003
[36] Wolfram, S.,. *Mathematica: A System for Doing Mathematics by Computer*, Addison Wesley, Reading, MA, 1988.
[37] Kundu, P. K., and Cohen, I. M., *Fluid Mechanics*, 2nd ed., Academic Press, San Diego, CA, 2002.
[38] Chang, F., and Dhir, V. K., "Mechanisms of Heat Transfer Enhancement and Slow Decay of Swirl in Tubes with Tangential Injection," *International Journal of Heat and Fluid Flow*, Vol. 16, No. 2, 1995, pp. 78–87. doi:10.1016/0142-727X(94)00016-6

J. Oefelein
Associate Editor